

Electronic Supplementary Information

for

A five-coordinate manganese(III) complex of a salen type ligand with a positive axial anisotropy parameter D

Sergiu Shova,^a Angelica Vlad,^a Maria Cazacu,^a J. Krzystek,^b Lukas Bucinsky,^c Martin Breza,^c Denisa Darvasiova,^c Peter Raptá,^c Joan Cano,^d Joshua Telser^{*e} and Vladimir B. Arion^{*f}

^aInorganic Polymers Department, “Petru Poni” Institute of Macromolecular Chemistry, Aleea Gr. Ghica Voda 41 A, Iasi 700487, Romania

^bNational High Magnetic Field Laboratory, Florida State University, Tallahassee, Florida 32310, USA

^cInstitute of Physical Chemistry and Chemical Physics, Slovak University of Technology, Radlinského 9, 81237 Bratislava, Slovak Republic

^dInstitut de Ciència Molecular, Universitat de València, Catedrático José Baltrán Martínez 2, 46980 Paterna, Spain

^eDepartment of Biological, Chemical and Physical Sciences, Roosevelt University, 430 S. Michigan Avenue, Chicago, Illinois 60605, USA

^fInstitute of Inorganic Chemistry of the University of Vienna, Währinger Strasse 42, A1090 Vienna, Austria

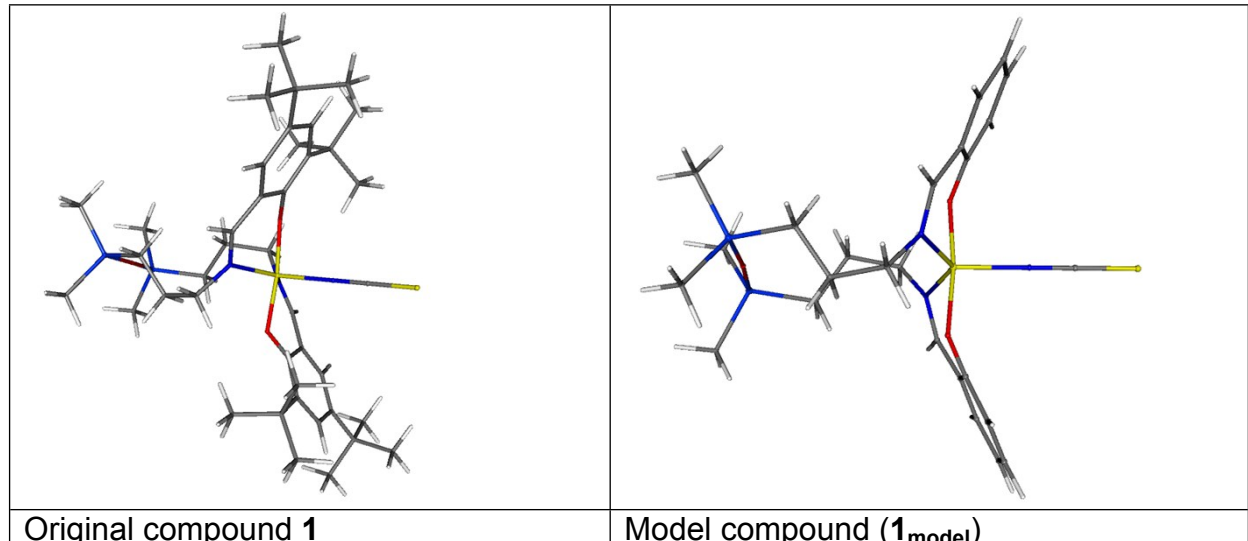


Figure S1. (a, left) original compound under study; (b, right) model compound.

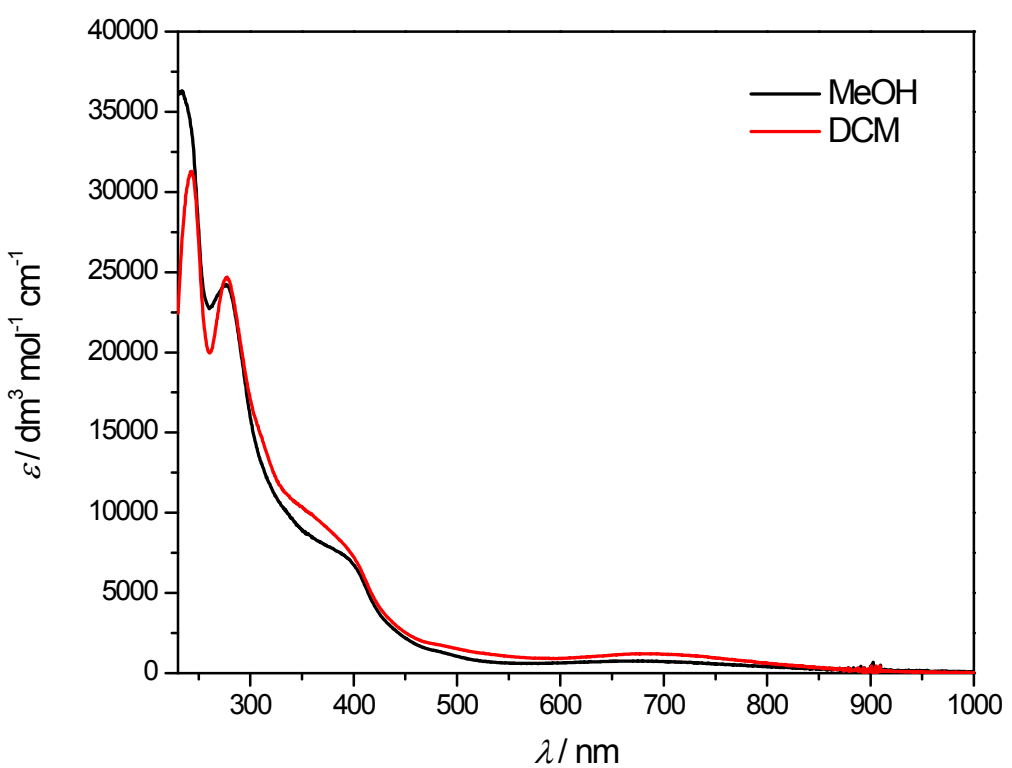


Figure S2. The UV-vis spectra of **1** in methanol and DCM.

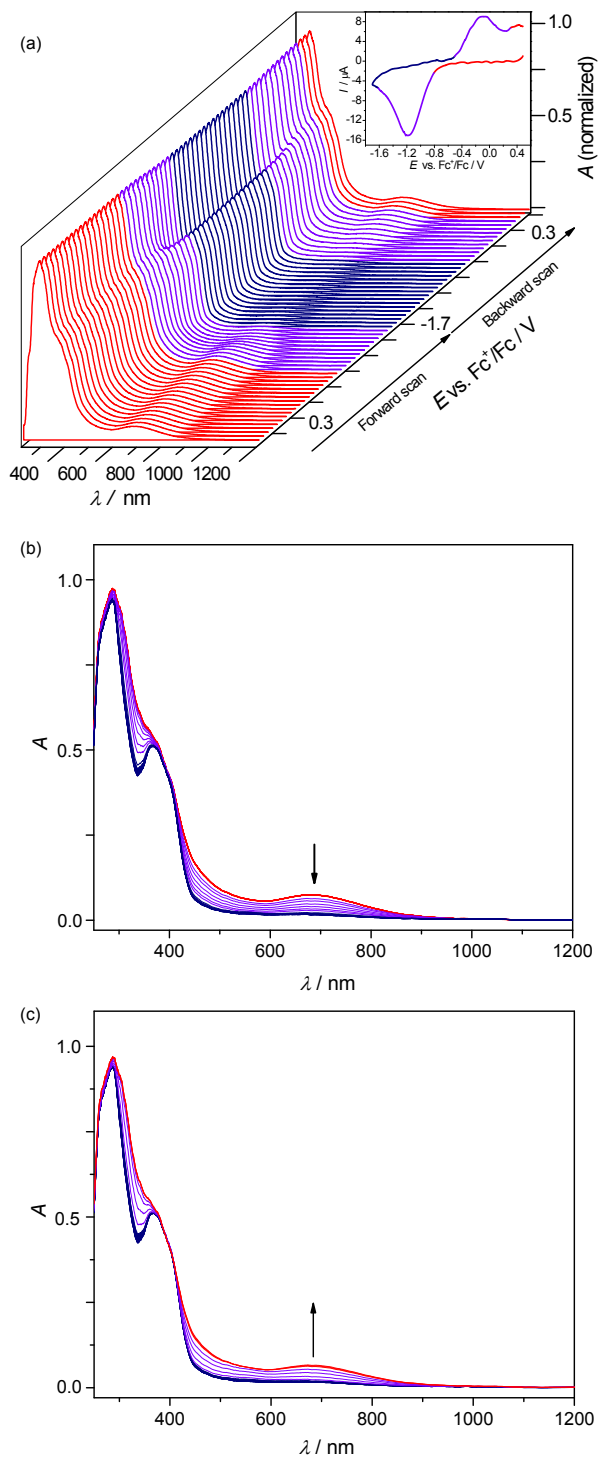


Figure S3. *In situ* UV-vis-NIR spectroelectrochemistry for **1** in 0.2 M n BuN₄[PF₆] in CH₂Cl₂ (scan rate of 5 mV s⁻¹, Pt-microstructured honeycomb working electrode): (a) UV-vis-NIR spectra detected simultaneously during the cyclic voltammetric scan (Inset: the corresponding cyclic voltammogram with colour-highlighted potential regions, where spectra were taken; (b) UV-vis-NIR spectra detected simultaneously upon the *in situ* reduction of **1** in the region of the first cathodic peak and (c) during the back reoxidation.

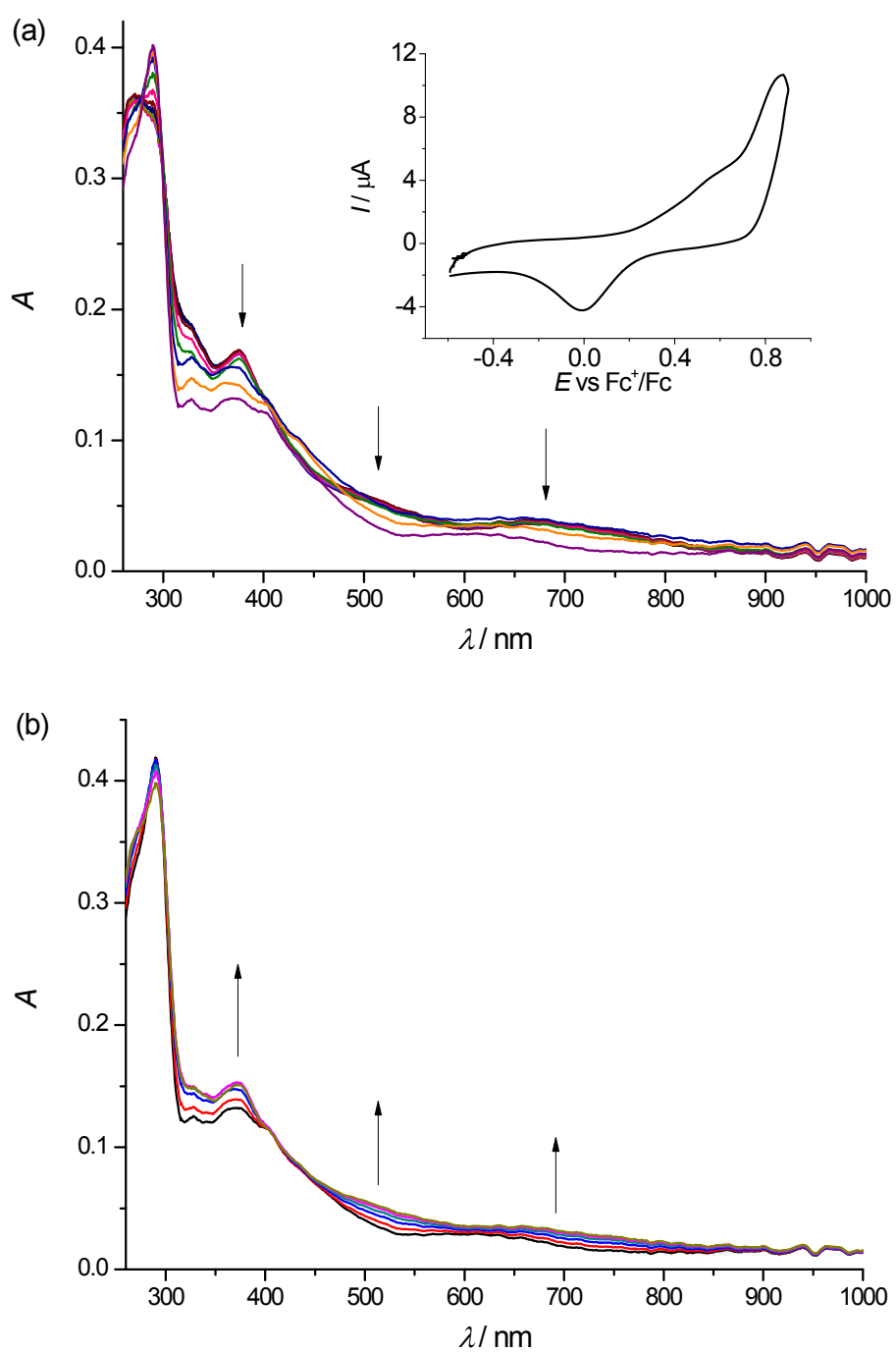


Figure S4. *In situ* optical spectroelectrochemistry for **1** in 0.2 M $n\text{BuN}_4[\text{PF}_6]$ in DCM (scan rate of 10 mV s $^{-1}$, Pt-microstructured honeycomb working electrode): UV-vis-NIR spectra recorded simultaneously upon (a) the *in situ* oxidation in the region of the first anodic peak (from -0.9 V to +0.9 V vs Fc^+/Fc) and upon (b) the back reduction in the region from +0.3 V to -0.6 V vs Fc^+/Fc . Inset in (a): the corresponding *in situ* cyclic voltammogram.

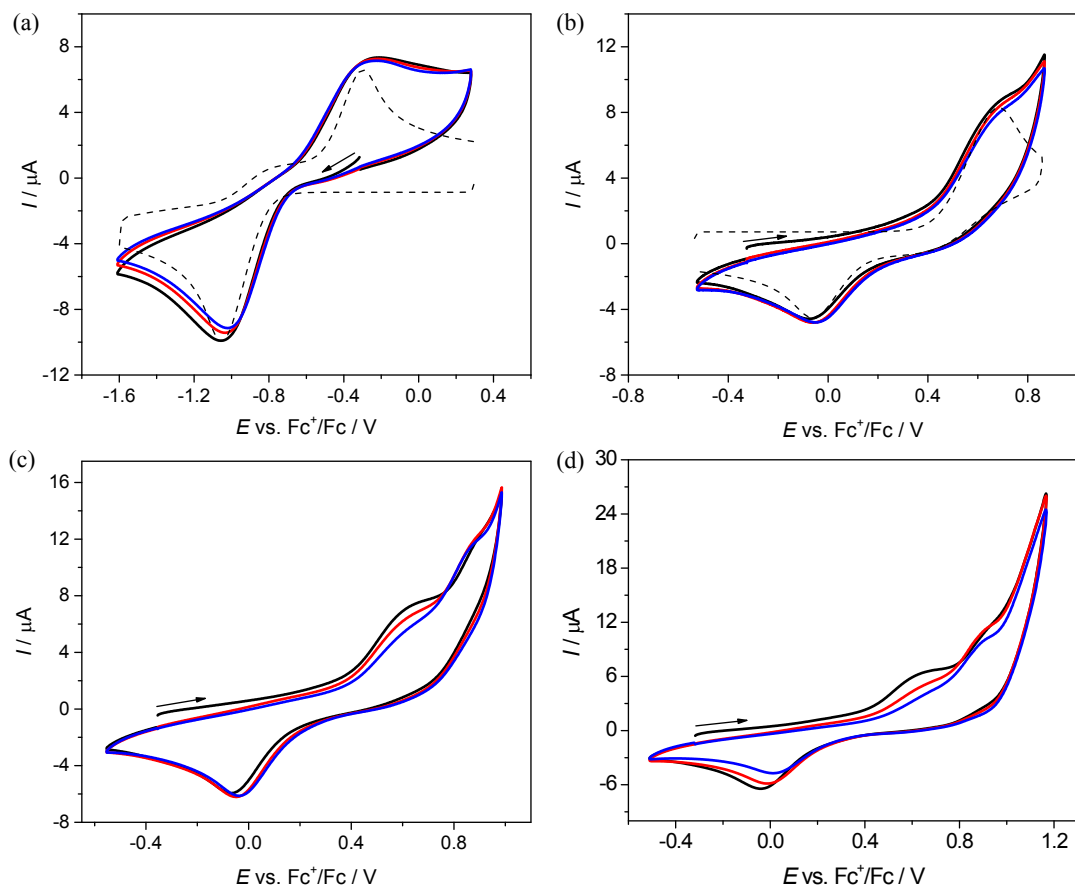


Figure S5. Cyclic voltammograms of **1** in $n\text{Bu}_4\text{NPF}_6/\text{CH}_2\text{Cl}_2$ (scan rate 20 mV s⁻¹, black line – the first voltammetric scan, red line – the second scan, blue line – the third scan) in the region (a) of the first cathodic peak, (b) of the first anodic peak as well as (c) going to the second oxidation step and (d) to the third anodic peak (dashed lines: estimated simulations using DigiElch Professional software from Gamry Instruments, version DigiElch8). Thin layer electrochemical cell with microstructured honeycomb working electrode was used.

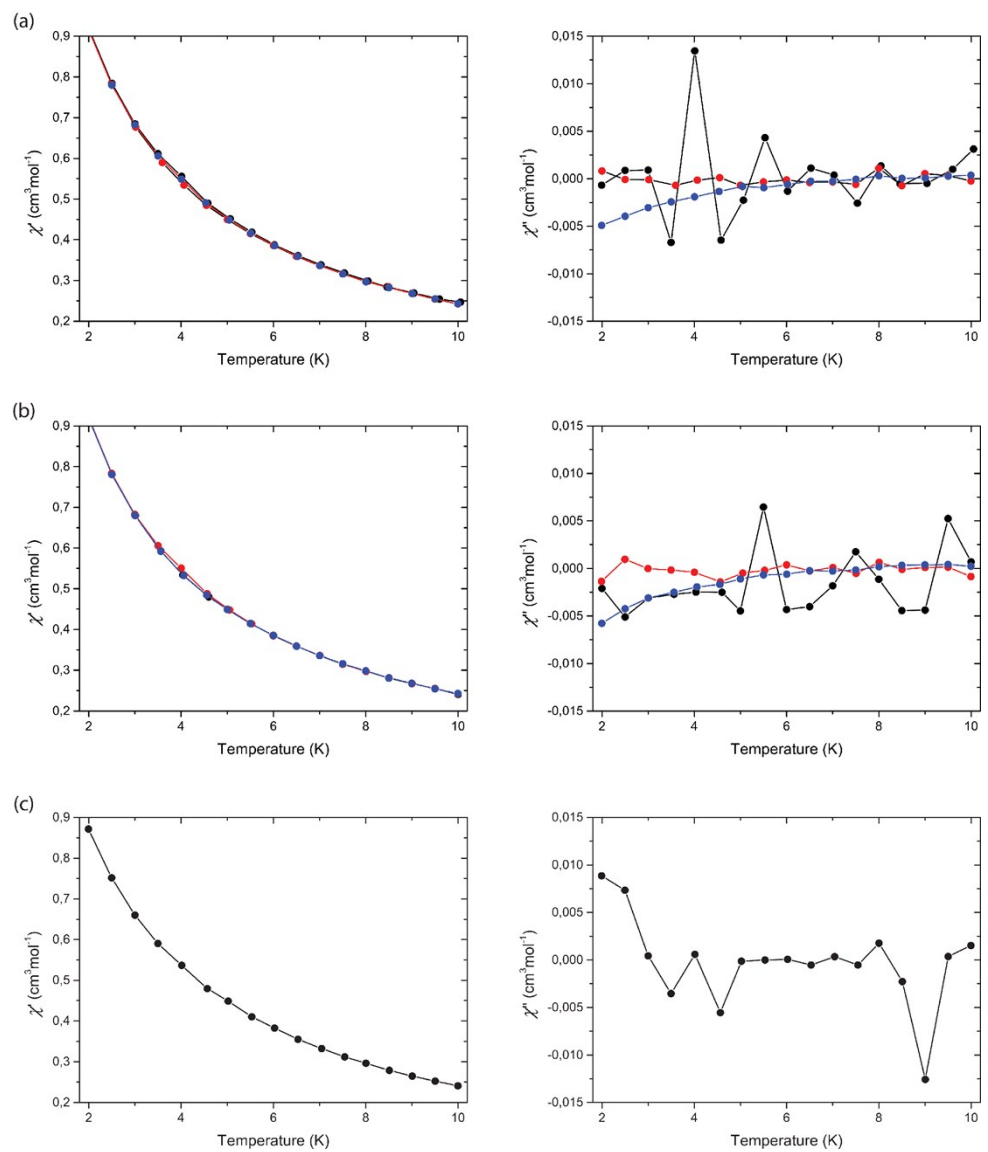


Figure S6. Temperature dependence of χ_M' (right) and χ_M'' (left) of **1** in a dc applied static field of 0.0 kG (a), 1.0 kG (b) and 2.5 kG (c) and under ± 4.0 G oscillating field at frequencies of 10 (blue), 100 (red) and 1000 Hz (black).

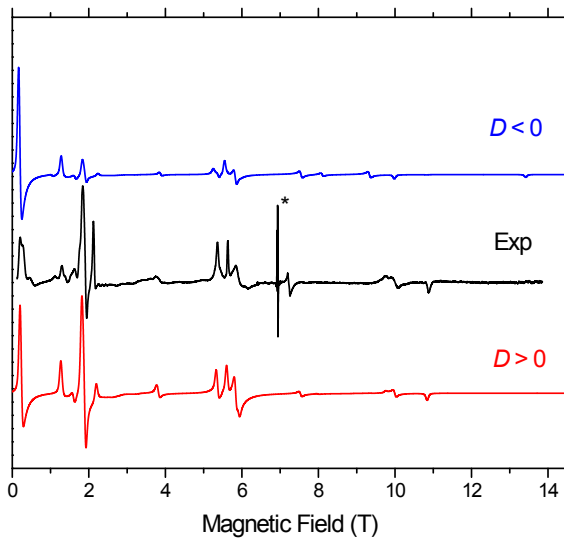


Figure S7. HFEPR spectrum of **1** at 201.6 GHz and 10 K (black trace) accompanied by simulations using spin Hamiltonian parameters as in Table 2. Blue trace: simulations using negative D ; red trace: positive D . The asterisk denotes a pair of signals at ca. 2.08 and 2.00 originating from an unknown impurity, and Mn^{II}, respectively. None of them is simulated.

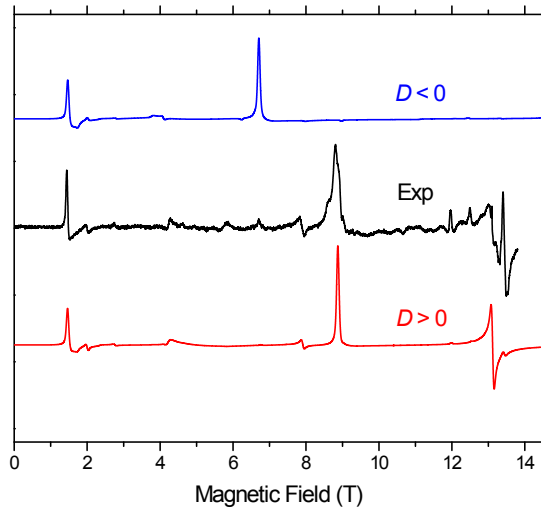


Figure S8. HFEPR spectrum of **1** at 412.8 GHz and 8 K (black trace) accompanied by simulations using spin Hamiltonian parameters as in Table 2. Blue trace: simulations using negative D ; red trace: positive D .

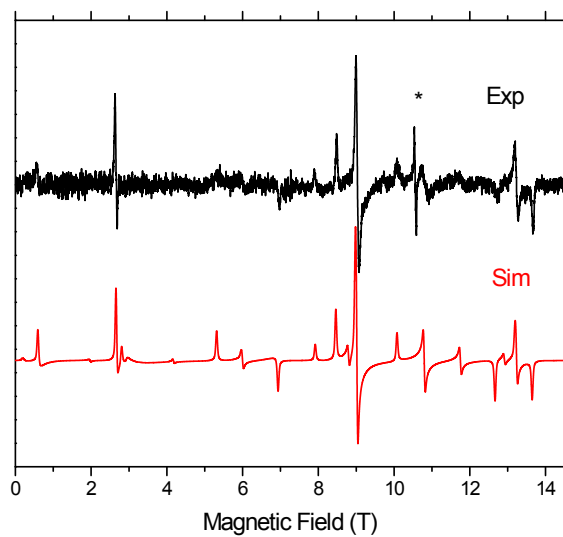


Figure S9. HFEPR spectrum of **1** at 295.2 GHz and 293 K (black trace) accompanied by simulations using spin Hamiltonian parameters as in Table 2. At this temperature, there is no difference between negative, and positive D , so the simulation (red trace) used positive D only.

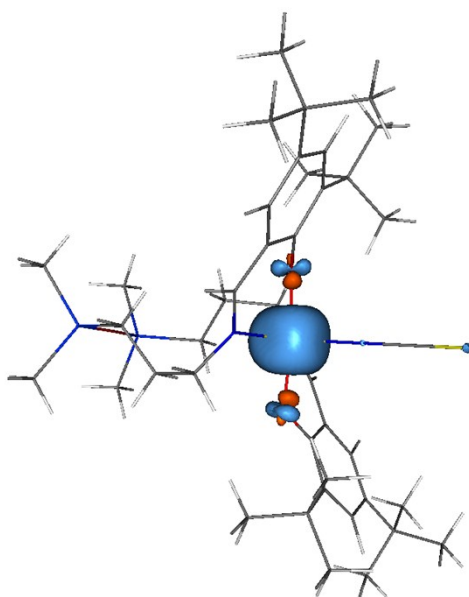
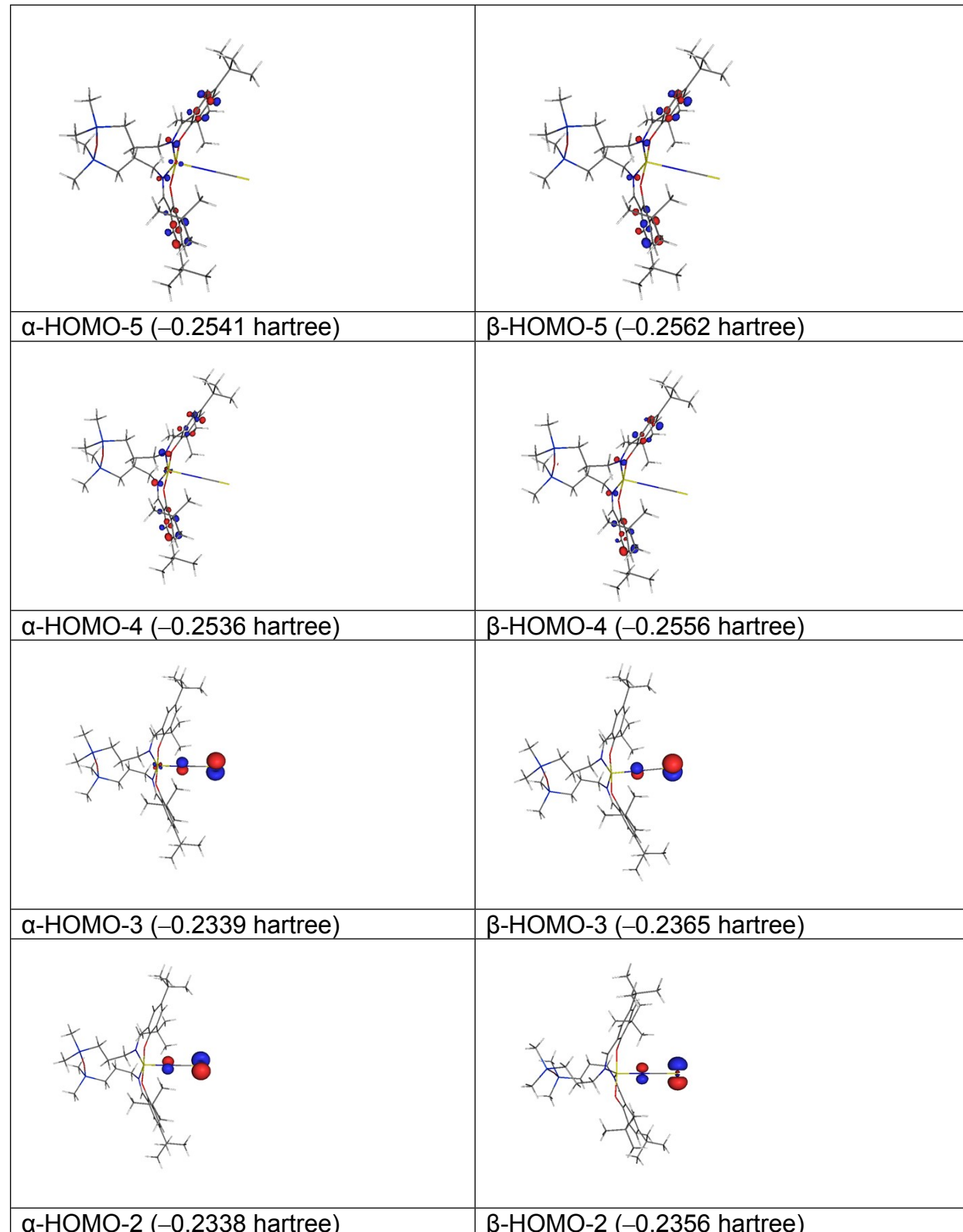
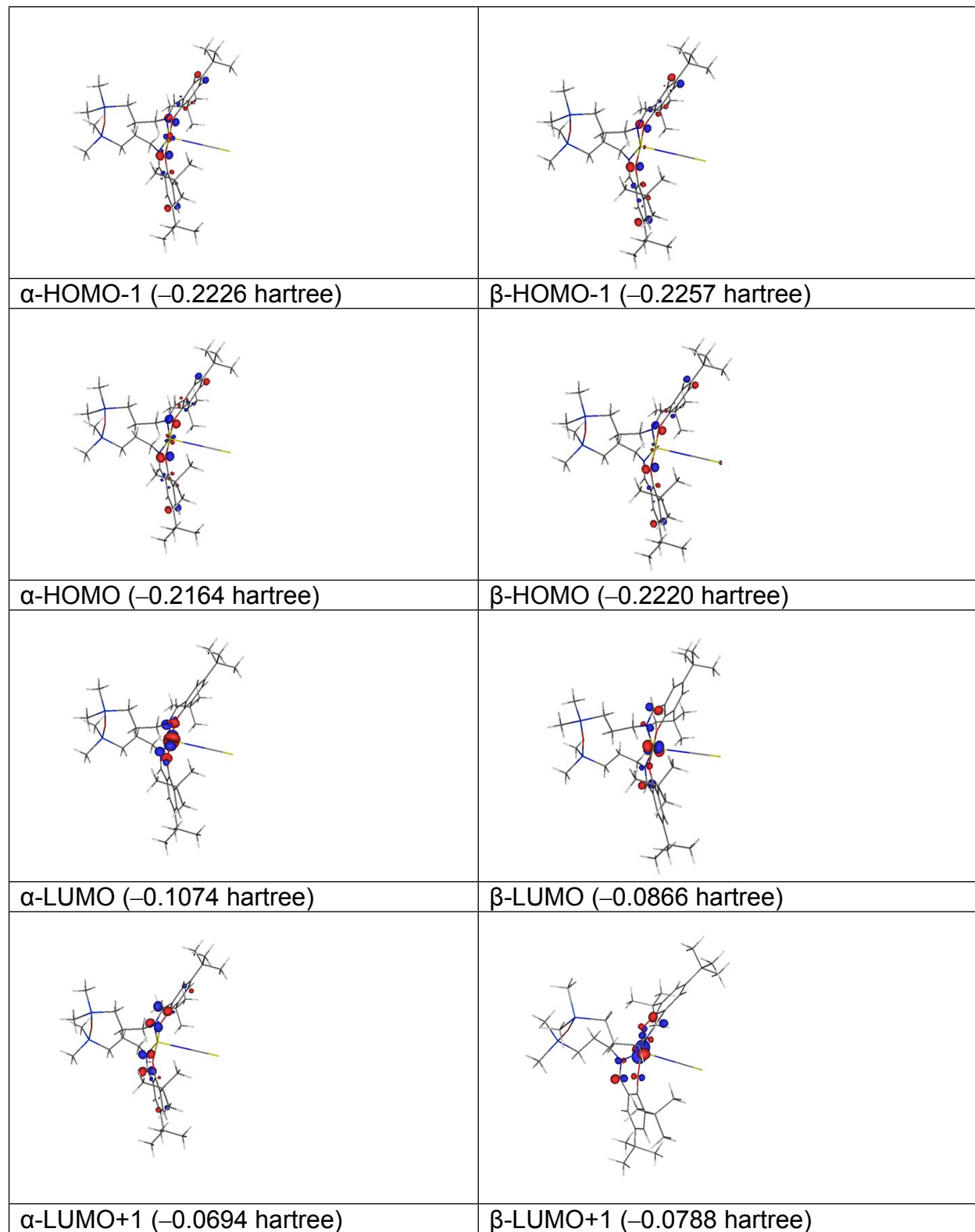


Figure S10. Spin density at ± 0.01 e/bohr 3 level for the DFT optimised geometry of **1** in the quintet spin state (blue, α spin; red, β spin density).





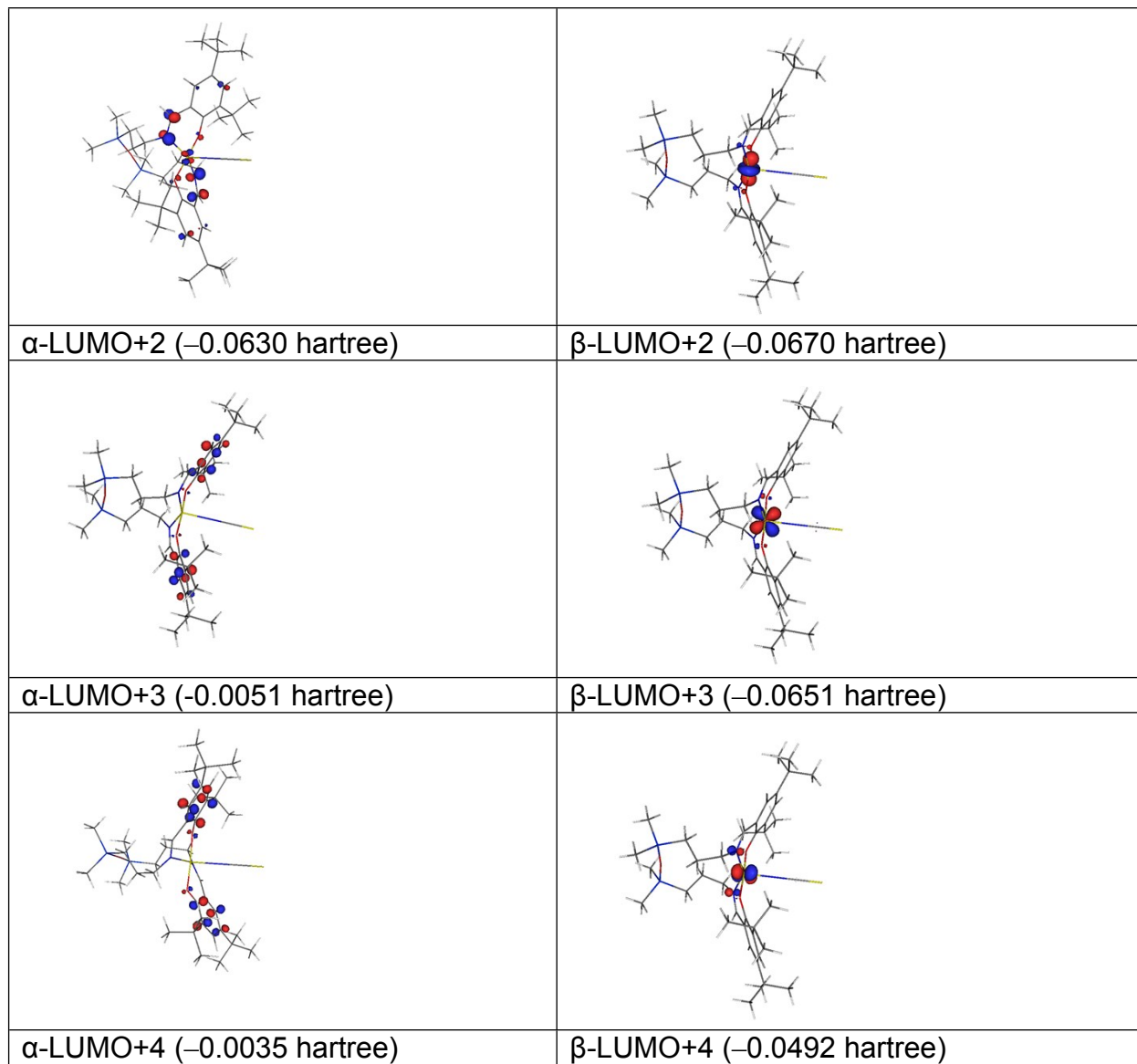


Figure S11. Frontier orbitals (drawn at 0.09 au level) of **1** in CH₃OH solution for DFT optimised geometry in the quintet spin state (orbital energies in parentheses).

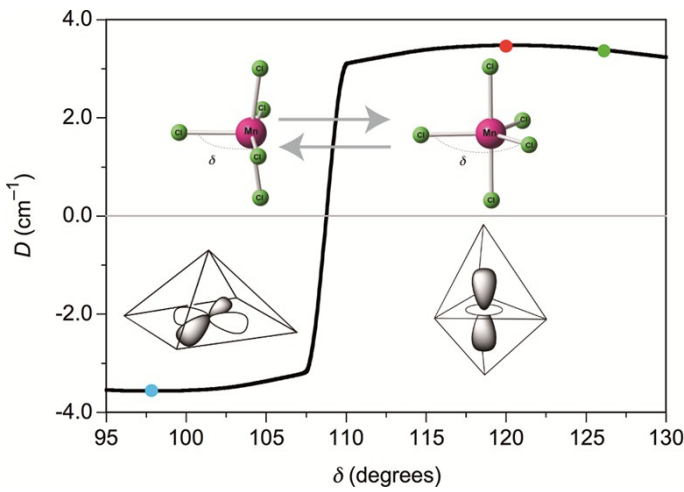


Figure S12. Geometrical dependence of D along the pathway connecting TBP and SPY geometries in $[\text{MnCl}_5]^{2-}$, as defined by the smallest $\text{Cl}-\text{Mn}-\text{Cl}$ angle, δ . The inset shows the sole empty d orbital for each geometrical conformation: z^2 (TBP) and xy (SPY) in the regions of positive and negative values of D , respectively. The horizontal grey line underlines the sign reversal of D . Cyan dot: optimised ideal SPY geometry. Two different bond lengths $\text{Mn}-\text{Cl}_{\text{ax}}$ and $\text{Mn}-\text{Cl}_{\text{eq}}$ were optimised, while the angle $\text{Cl}_{\text{ax}}\text{Mn}\text{Cl}_{\text{eq}}$ was fixed at 90 deg; Red dot: optimised ideal TBP geometry. Two bond lengths $\text{Mn}-\text{Cl}_{\text{ax}}$ and $\text{Mn}-\text{Cl}_{\text{eq}}$ were optimised, while the angles $\text{Cl}_{\text{ax}}\text{Mn}\text{Cl}_{\text{eq}}$ and $\text{Cl}_{\text{eq}}\text{Mn}\text{Cl}_{\text{eq}}$ were fixed at 90 and 120 deg, respectively; Green dot: The geometry represented by the red dot was again optimised, but unfreezing the $\text{Cl}_{\text{ax}}\text{Mn}\text{Cl}_{\text{eq}}$ and $\text{Cl}_{\text{eq}}\text{Mn}\text{Cl}_{\text{eq}}$ angles. This geometry is less stable than the ideal TBP due to undergoing a distortion within the basal plane similar to that observed in **1**, namely the two $\text{Cl}_{\text{eq}}\text{Mn}\text{Cl}_{\text{eq}}$ angles are above 120 deg. Thus this result, which corresponds to the properly idealised reference geometry in the shape framework is similar to that given by the red dot, having the same axial and equatorial bond lengths, and validates the overestimation of the contribution of a SPY geometry found from the shape calculations.

Table S1. Bond lengths [Å] and angles [°] for **1** obtained by X-ray experiment and by DFT optimisation (significant differences in bold).

Atom1-Atom2	X-ray	DFT	Atom1-Atom2	X-ray	DFT
Mn-O1	1.867(4)	1.881	C5-C6	1.398(9)	1.410
Mn-O2	1.859(4)	1.881	C6-C15	1.446(10)	1.439
Mn-N1	2.065(6)	2.105	C7-C8	1.520(9)	1.546
Mn-N2	2.033(5)	2.104	C7-C9	1.558(9)	1.541
Mn-N3	2.032(7)	1.976	C7-C10	1.502(10)	1.546
S1-C41	1.609(10)	1.615	C11-C12	1.518(9)	1.539
Si1-O3	1.596(7)	1.654	C11-C13	1.541(11)	1.545
Si1-C18	1.858(8)	1.892	C11-C14	1.534(11)	1.546
Si1-C19	1.831(9)	1.882	C16-C17	1.509(11)	1.537
Si1-C20	1.867(10)	1.881	C17-C18	1.520(10)	1.536
Si2-O3	1.620(7)	1.654	C23-C24	1.534(10)	1.536
Si2-C21	1.846(10)	1.881	C24-C25	1.489(10)	1.537
Si2-C22	1.840(10)	1.882	C26-C27	1.449(10)	1.439
Si2-C23	1.846(8)	1.892	C27-C28	1.407(10)	1.410
O1-C1	1.347(8)	1.326	C27-C32	1.409(9)	1.421
O2-C32	1.332(8)	1.327	C28-C29	1.364(11)	1.380
N1-C15	1.282(9)	1.292	C29-C30	1.416(12)	1.411
N1-C16	1.471(8)	1.466	C29-C37	1.522(12)	1.537
N2-C25	1.501(9)	1.466	C30-C31	1.356(11)	1.391
N2-C26	1.271(9)	1.292	C31-C32	1.428(10)	1.428
N3-C41	1.145(10)	1.183	C31-C33	1.537(11)	1.542
C1-C2	1.396(9)	1.428	C33-C34	1.518(11)	1.545
C1-C6	1.413(9)	1.421	C33-C35	1.537(11)	1.546
C2-C3	1.395(10)	1.391	C33-C36	1.526(12)	1.539
C2-C7	1.543(9)	1.542	C37-C38	1.522(9)	1.546
C3-C4	1.394(10)	1.411	C37-C39	1.542(11)	1.546
C4-C5	1.353(10)	1.380	C37-C40	1.538(11)	1.541
C4-C11	1.512(10)	1.537			
O1-Mn-N1	87.7(2)	86.2	C8-C7-C9	106.6(6)	107.1
O1-Mn-N2	89.9(2)	91.1	C10-C7-C2	111.1(6)	110.8
O1-Mn-N3	92.9(2)	93.7	C10-C7-C8	107.0(6)	106.9
O2-Mn-O1	173.1(2)	172.7	C10-C7-C9	111.7(6)	110.7
O2-Mn-N1	90.0(2)	91.1	C4-C11-C12	111.1(7)	109.7
O2-Mn-N2	87.8(2)	86.2	C4-C11-C13	108.2(10)	109.5
O2-Mn-N3	94.1(3)	93.7	C4-C11-C14	112.0(10)	112.1
N2-Mn-N1	141.0(2)	136.5	C12-C11-C13	100.4(12)	108.0
N3-Mn-N1	107.7(3)	111.8	C12-C11-C14	118.7(13)	109.3
N3-Mn-N2	111.3(3)	111.7	C14-C11-C13	105.1(13)	108.0
O3-Si1-C18	107.6(4)	108.2	N1-C15-C6	128.7(7)	127.4
O3-Si1-C19	111.4(4)	109.5	N1-C16-C17	111.3(6)	112.3
O3-Si1-C20	108.6(5)	109.0	C16-C17-C18	115.8(6)	114.4
C18-Si1-C20	109.3(4)	110.9	C17-C18-Si1	116.1(6)	115.8
C19-Si1-C18	109.3(4)	109.2	C24-C23-Si2	114.8(6)	115.8
C19-Si1-C20	110.7(5)	110.1	C25-C24-C23	114.6(6)	114.4
O3-Si2-C21	109.1(5)	109.0	C24-C25-N2	112.1(6)	112.3
O3-Si2-C22	109.4(4)	109.5	N2-C26-C27	126.6(7)	127.3
O3-Si2-C23	105.9(4)	108.2	C28-C27-C26	117.6(7)	117.3
C21-Si2-C23	111.6(4)	110.9	C28-C27-C32	121.2(7)	121.0
C22-Si2-C21	108.6(5)	110.1	C32-C27-C26	121.0(6)	121.7
C22-Si2-C23	112.2(5)	109.2	C29-C28-C27	121.1(8)	121.5
C1-O1-Mn	126.5(4)	125.4	C28-C29-C30	116.0(8)	116.4
C32-O2-Mn	124.3(4)	125.4	C28-C29-C37	123.4(8)	123.7

Si1-O3-Si2	163.5(5)	173.7	C30-C29-C37	120.6(8)	119.9
C15-N1-Mn	120.4(5)	119.2	C31-C30-C29	126.4(8)	125.2
C15-N1-C16	118.4(6)	118.2	C30-C31-C32	116.8(7)	117.3
C16-N1-Mn	121.2(5)	122.3	C30-C31-C33	122.0(7)	121.1
C25-N2-Mn	120.4(4)	122.3	C32-C31-C33	121.2(7)	121.6
C26-N2-Mn	121.4(5)	119.2	O2-C32-C27	120.3(6)	120.1
C26-N2-C25	118.2(6)	118.2	O2-C32-C31	121.0(6)	121.3
C41-N3-Mn	167.0(7)	179.9	C27-C32-C31	118.5(7)	118.4
O1-C1-C2	120.4(6)	121.3	C34-C33-C31	110.7(6)	110.8
O1-C1-C6	120.5(6)	120.1	C34-C33-C35	105.7(7)	108.8
C2-C1-C6	119.0(6)	118.5	C34-C33-C36	111.9(8)	112.4
C1-C2-C7	122.0(6)	121.6	C35-C33-C31	111.7(7)	110.7
C3-C2-C1	116.9(7)	117.3	C36-C33-C31	108.8(7)	106.9
C3-C2-C7	121.1(6)	121.1	C36-C33-C35	108.1(7)	107.2
C4-C3-C2	125.0(7)	125.2	C29-C37-C38	111.5(8)	109.7
C3-C4-C11	119.9(7)	119.9	C29-C37-C39	105.2(12)	109.5
C5-C4-C3	116.8(7)	116.4	C29-C37-C40	112.4(14)	112.1
C5-C4-C11	123.3(7)	123.7	C38-C37-C39	94.7(14)	108.0
C4-C5-C6	121.5(7)	121.5	C38-C37-C40	116.2(16)	109.3
C1-C6-C15	120.5(6)	121.7	C39X-C37-C29	115.3(12)	-
C5-C6-C1	120.8(7)	121.0	C39X-C37-C38	119.6(15)	-
C5-C6-C15	118.5(6)	117.3	C40-C37-C39	115.2(15)	108.0
C2-C7-C9	108.0(6)	108.8	N3-C41-S1	179.6(10)	180.0
C8-C7-C2	112.5(6)	112.4			

Table S2. Calculated ZFS parameters (6-311G* basis set) for the model compound (**1_{model}**), optimal B3LYP/6-311G* geometry used.

THEORY	D (cm ⁻¹)	E (cm ⁻¹)	g _x	g _y	g _z
CASSCF(4,5)	2.189	0.156	1.999	2.000	2.000
sa-CASSCF(4,5)	2.859	0.148	1.974	1.976	2.000
sa-NEVPT2(4,5)	2.893	0.154	1.978	1.979	2.000
sa-MRCI(4,5)	3.348	0.187			
BLYP	1.172	0.112	1.995	1.996	2.004

Table S3. DFT calculated spin squares ($\langle S^2 \rangle$), DFT energies (E_{DFT}), free energies at 298 K (G₂₉₈).

Spin S	1	2	3 ^a
Unrestricted formalism			
$\langle S^2 \rangle$	2.023	6.052	12.017
E _{DFT} [hartree]	-4121.02002	-4121.06182	-4121.02336
G ₂₉₈ [hartree]	-4120.11676	-4120.16444	-4120.13490
Restricted formalism			
E _{DFT} [hartree]	-4121.01715	-4121.05598	-4121.01947
G ₂₉₈ [hartree]	-4120.11388	-4120.15859	-4120.13101

^aAdditional spin density is located at sulfur, oxygens and neighbouring phenyl rings.

Table S4. Relevant NBO electron structure parameters of **1** in various spin states.

Spin multiplicity	3	5	7 ^a
Natural atomic charge			
Mn	1.523	1.747	1.626
O1	-0.756	-0.771	-0.762
O2	-0.756	-0.771	-0.759
N1	-0.558	-0.603	-0.615
N2	-0.558	-0.603	-0.616
N3	-0.646	-0.779	-0.743
C41	0.180	0.192	0.164
S	-0.201	-0.189	-0.140
d-electron population			
Mn	5.21	4.97	5.13
Unpaired electron density			
Mn	1.953	3.801	4.646
O1	0.034	0.002	0.161
O2	0.034	0.002	0.162
N1	-0.017	0.007	0.058
N2	-0.017	0.007	0.048
N3	-0.036	0.226	0.059
C41	0.007	0.025	0.006
S	0.050	0.073	0.186
Overlap weighted NAO bond order			
Mn – O1	0.304	0.289	0.120
Mn – O2	0.302	0.289	0.118
Mn – N1	0.263	0.210	0.146
Mn – N2	0.263	0.210	0.146
Mn – N3	0.388	0.283	0.197

^a Additional spin density is located at sulfur, oxygens and neighbouring phenyl rings.

Table S5. Most intense calculated electron transitions for **1** in methanol in quintet spin state.

Excitation energy [eV]	Wavelength [nm]	Oscillator strength	Relevant contributions
3.524	352	0.12	$\beta\text{-HOMO-1} \rightarrow \beta\text{-LUMO+3}$ $\alpha\text{-HOMO-4} \rightarrow \alpha\text{-LUMO}$ $\alpha\text{-HOMO-1} \rightarrow \alpha\text{-LUMO+1}$
4.246	292	0.14	$\alpha\text{-HOMO-5} \rightarrow \alpha\text{-LUMO+1}$ $\beta\text{-HOMO-5} \rightarrow \beta\text{-LUMO+2}$ $\beta\text{-HOMO-4} \rightarrow \beta\text{-LUMO}$ $\beta\text{-HOMO} \rightarrow \beta\text{-LUMO+5}$
4.483	277	0.15	$\alpha\text{-HOMO-5} \rightarrow \alpha\text{-LUMO+1}$ $\beta\text{-HOMO-5} \rightarrow \beta\text{-LUMO+2}$
4.685	265	0.28	$\beta\text{-HOMO} \rightarrow \beta\text{-LUMO+6}$ $\beta\text{-HOMO-8} \rightarrow \beta\text{-LUMO+2}$
4.967	250	0.14	$\alpha\text{-HOMO-6} \rightarrow \alpha\text{-LUMO+1}$ $\beta\text{-HOMO-4} \rightarrow \beta\text{-LUMO+4}$
5.408	229	0.15	$\alpha\text{-HOMO} \rightarrow \alpha\text{-LUMO+4}$ $\beta\text{-HOMO-8} \rightarrow \beta\text{-LUMO+5}$
5.474	227	0.10	$\alpha\text{-HOMO-1} \rightarrow \alpha\text{-LUMO+3}$ $\beta\text{-HOMO-11} \rightarrow \beta\text{-LUMO}$
5.528	224	0.15	$\beta\text{-HOMO-11} \rightarrow \beta\text{-LUMO}$ $\beta\text{-HOMO-9} \rightarrow \beta\text{-LUMO+2}$ $\beta\text{-HOMO} \rightarrow \beta\text{-LUMO+8}$